JOURNAL OF GEOPHYSICAL RESEARCH, VOL. 115, A04214, doi:10.1029/2009JA014630, 2010

Interaction of Saturn's magnetosphere and its moons: 1. Interaction between corotating plasma and standard obstacles

Y.-D. Jia,[1] C. T. Russell,[1,2] K. K. Khurana,[1] G. Toth,[3] J. S. Leisner,[1,4] and T. I. Gombosi[3]

Received 7 July 2009; revised 10 November 2009; accepted 17 November 2009; published 27 April 2010.

[1] The interaction of Saturn's inner magnetosphere with its moons ranges from the addition of significant quantities of gas, dust, and plasma, causing significant consequences for the dynamics and energetics of the entire Saturnian magnetosphere, to the simple absorption of plasma and energetic particles by the icy moons with non-electrically conducting interiors. The interaction with these moons is complex with the contribution of many physical processes, depending on the geometry of any plume, the structure of the atmosphere, and its interaction with the surface and interior of the moon, the latter by induced fields. Our ultimate goal is to understand the complexities of this interaction and its temporal variations, especially at Enceladus. In this paper we use magnetohydrodynamics (MHD) code for addressing the flow around obstacles that are simpler than the Enceladus interaction. These simulations both help us understand the interaction with other icy moons and prepare us for the simulation of the flow around Enceladus. The processes involved include ordinary collisions, impact ionization, photoionization, and charge exchange. We examine a series of simple canonical interactions before we later apply our simulation where the multiple processes are occurring simultaneously with asymmetric geometries. We apply our 3-D MHD model to simulate the interaction between the Saturnian corotational plasma flow for the following cases: an absorbing body having an insulating surface; ion pickup via photo and impact ionization from a spherically symmetric neutral cloud; charge exchange with such a neutral cloud; and ion pickup at an insulating, absorbing body with an atmosphere acted upon by the sum of the three ionization processes. In addition to validating the model and obtaining a deeper understanding of the consequences of each interaction, we can immediately make some conclusions about the Enceladus interaction. We find that the magnetometer data are most consistent with the surface of Enceladus being absorbing and insulating, rather than the surface being reflecting and electrically conducting. For the conditions in the corotating flow at Enceladus, the perturbation to the plasma flow produced by photo/impact ionization is an order of magnitude smaller than that produced by charge exchange. Moreover, the perturbation to the magnetic field B_z component by a spherically symmetric mass loading source alone is an order of magnitude smaller than that observed in the neighborhood of the plume. Thus, the perturbation observed in the magnetometer data is primarily due to the mass loading in the plume, which is primarily ion-neutral charge exchange. The geometry and source strength of the plume are investigated in a following paper.

Citation: Jia, Y.-D., C. T. Russell, K. K. Khurana, G. Toth, J. S. Leisner, and T. I. Gombosi (2010), Interaction of Saturn's magnetosphere and its moons: 1. Interaction between corotating plasma and standard obstacles, *J. Geophys. Res.*, *115*, A04214, doi:10.1029/2009JA014630.

1. Introduction

[2] One of the Saturnian icy moons, Enceladus (radius $R_E \sim 250$ km), orbits at 3.95 Saturn radii with a speed of 12.6 km/s. It is accompanied by a plasma torus, composed mostly of water group ions [*Richardson et al.*, 1998] that corotate with the planet at a speed of 39 km/s, resulting in a net flow speed of 26.4 km/s relative to Enceladus [e.g., *Burger et al.*, 2007]. Cassini has made seven close flybys to Enceladus in 2005 and 2008. These studies confirm the

[1]IGPP, University of California, Los Angeles, California, USA.
[2]Department of Earth and Space Science, University of California, Los Angeles, California, USA.
[3]Department of Atmospheric, Oceanic and Space Sciences, University of Michigan, Ann Arbor, Michigan, USA.
[4]Department of Physics and Astronomy, University of Iowa, Iowa City, Iowa, USA.

0148-0227/10/2009JA014630

Table 1. Summary of Four Cases Presented in This Study

Case	Body	Photo/Impact Ionization	Charge Exchange
1	yes	no	no
2	no	yes	no
3	no	no	yes
4	yes	yes	yes

extensive gas plume at the moon's south pole. Such a plume injects gas particles at a rate of approximately 10^{28} s^{-1} [*Waite et al.*, 2006; *Hansen et al.*, 2006] into the inner Saturnian system, which is eventually ionized and added to the plasma disk of the Saturnian magnetosphere [*Dougherty et al.*, 2006; *Kivelson*, 2006].

[3] The newly ionized neutral particles are picked up by the rapidly corotating Saturnian plasma. The major ionization processes can be grouped into three types: photoionization, electron impact ionization and ion-neutral charge exchange. Among these, photo and impact ionizations create fresh electrons, while charge exchange does not. Thus the photo/impact ionizations can also be called electron-creating ionizations. The combination of these three ion pickup processes modifies the mass and momentum of the interacting plasma flow, so their effect is considered mass loading to the plasma.

[4] The dynamic plasma environment at Enceladus is comparable with that of Io [*Delamere et al.*, 2007; *Vasyliunas*, 2008], the geologically active Jovian moon that ejects SO_2 gas into its torus at a comparable rate of 3×10^{28} s^{-1} [e.g., *Saur et al.*, 2002; *Lipatov and Combi*, 2006]. However, the mass loading character of these two worlds and their effects on these global planetary magnetospheres differ, not only because of the geometry of the interaction region, but also because of the ionization rates of the liberated gas.

[5] Around Io, almost a ton of corotating ions is added per second into its torus [e.g., *Bagenal*, 1997], while at Enceladus, the new ion production is barely 3 kg/s [*Khurana et al.*, 2007]. Nevertheless the effects of these different rates are more comparable when the strength of the magnetic field near the two moons is considered: about three grams of picked-up ions per Weber of flux tubes convected across the diameter of Io and almost one gram of ions per Weber at Enceladus. Thus the added ions are almost as important for the dynamics of the Saturnian magnetosphere as the Io-genic ions are for the Jovian magnetosphere.

[6] In terms of chemical reactions, the Enceladus environment has similarities to a cometary atmosphere which is also dominated by water group particles [*Haberli et al.*, 1997; *Jia et al.*, 2008], but unlike a comet, the incoming flow is dominated by water group ions rather than protons. At both objects, the charge-exchange interaction has important consequences as it removes momentum from the flow that is returned to the new ions from the surrounding plasma through the stress of the bent and compressed magnetic field resulting from the interaction. However, around a comet with a heliocentric distance around 1 AU, photoionization is about two orders of magnitude stronger than that around Enceladus, and thus contributes significantly to the pickup ions. At Enceladus the pickup ions are created primarily by charge exchange between water group ions and neutrals, which results in momentum change only. In addition, the relative energy of the water group ions and neutrals are different between these two worlds, and thus a more accurate investigation of such chemical reactions requires multispecies or even multifluid methods considering the different rate of charge-exchange reactions at different relative speeds between ions and neutrals.

[7] Much was learned about the neutral plume from the observations during the E2 flyby [e.g., *Waite et al.*, 2006; *Tokar et al.*, 2006; *Saur et al.*, 2008]. (The naming convention of the flybys is to use the first letter of the moon (in this case E for Enceladus) and append the sequence number starting from 0.) From these studies, the plume is estimated to be centered at the south pole, with a latitudinal distribution of 10°~15° [*Porco et al.*, 2006; *Spitale and Porco*, 2007]. The strength of the mass loading process, as revealed by the Cassini magnetometer data on the first three flybys, has been estimated by *Khurana et al.* [2007] with a Biot-Savart modeling method. They obtained a plasma loading rate of 10^{26} ions/s in the vicinity of Enceladus. *Saur et al.* [2008] obtained a mass loading rate of 0.2~3 kg/s (10^{25}~10^{26} ions/s) using a two-fluid plasma interaction model. As indicated by the Monte Carlo model of *Burger et al.* [2007], an ion mass loading rate of 10^{26} s^{-1} within the plume corresponds to a neutral gas production of 10^{28} s^{-1}. The electron-creating ionization rate that *Burger et al.* [2007] used is 0.8×10^{-8} s^{-1}, while the average charge-exchange rate is approximately 4×10^{-15} $m^3 s^{-1}$. In this paper we use a larger impact ionization rate, as suggested by the CAPS observations, and a smaller charge exchange rate, as calculated with a lower relative velocity between ions and neutrals. A density-dependent impact ionization rate and a velocity-dependent charge exchange rate will be discussed in future works.

[8] *Saur et al.* [2007] introduced a current system tangential to the Enceladus surface to couple the ionospheres in the southern and northern hemispheres of Saturn. It is found that the body-plume system at Enceladus forms a unique interaction with the magnetospheric plasma of Saturn. Its significance for the dynamics of the magnetosphere is comparable to that of the Io-Jupiter interaction, given the lower magnetic moment and smaller dynamic pressure of the solar wind at Saturn.

[9] In this paper, we present results of numerical simulations with simple geometries and specific models of the interaction and discuss their physical implications to set the foundation for our later study of the Enceladus plume and to provide a basis for comparison of the interactions with other moons, especially the Earth's Moon, Jupiter's Io, as well as Saturn's Tethys, Dione and Rhea. As summarized in Table 1, four typical cases are investigated to compare the interactions due to surface absorption, photo/impact ionization, charge exchange and the combined effect of these three.

[10] The torus-Enceladus interaction region can be considered to be a combination of three interactions: that of the flowing plasma with the plume, that with the absorbing surface of Enceladus, and that with the sputtering-produced atmosphere [*Jurac et al.*, 2001] of Enceladus. The self-consistent simulations of the interaction with the atmosphere, surface and plume are presented in an accompanying paper [*Jia et al.*, 2010]. With the objective of comparing our modeling results for all seven Cassini flybys in 2005 and 2008, the third study is targeted at the determination of the

time variation of the Enceladus plume between 2005 and 2008 (Y.-D. Jia et al., Interaction of Saturn's magnetosphere and its moons: 3. Time variation of the Enceladus plume, manuscript in preparation, 2010). Here we begin by describing the model and plasma parameters used in these studies, followed by a description and discussion of the results along with their summary.

2. Model Description

[11] The interaction between the magnetospheric plasma and a gas-producing moon is characterized by a complex system involving a submagnetosonic plasma flow, the corotating planetary magnetic field, the newly picked-up plasma around the moon, the ejected neutral particles, and the planetary surface. For the current stage we simplify this multifluid interaction into a single-fluid single-species interaction model, by treating the ion pickup as source terms added to our MHD equations.

[12] The saturnian magnetic field strength is approximately 330 nT at the Enceladus orbit, as determined using the Cassini magnetometer [*Dougherty et al.*, 2006]. Pickup water ions have a gyro radius of approximately r_g = 10 km (0.04 R_E) in this magnetic field, which is smaller than the scale of the moon and the plume. Such an interaction in the cold plasma is applicable for MHD simulations, while for other moons in the outer magnetosphere including Titan, the gyro radius increases, so hybrid simulations are necessary for comparisons. As examples, $r_g \approx 0.1$ R_D at Dione, while $r_g \approx 1$ R_T at Titan.

[13] This study applies an icy-moon version of the (Block Adaptive Tree Solar-wind Roe Upwind Scheme) BATS-R-US, a 3-D MHD code developed and maintained at the University of Michigan [*Powell et al.*, 1999; *Tóth et al.*, 2005]. In this section we present our governing equations and the boundary conditions to be used.

2.1. Mass-Loaded MHD Equations

[14] The governing equations in this model are the mass-loaded ideal MHD equations [e.g., *Jia et al.*, 2007]. This code, with its multiscale grid system, has been applied to various plasma environments [e.g., *Kabin et al.*, 2000; *Ma et al.*, 2006]. The normalized equations can be written compactly as done by *Gombosi et al.* [1996]:

$$\frac{\partial \mathbf{W}}{\partial t} + (\nabla \cdot \mathbf{F})^T = \mathbf{P}, \tag{1}$$

with the state vector $\mathbf{W}$ defined as the following:

$$\mathbf{W} = (\rho, \rho\mathbf{u}, \mathbf{B}, \varepsilon)^T \tag{2}$$

In the definition above, ρ is the plasma density, $\mathbf{u}$ and $\mathbf{B}$ are the velocity and magnetic field vectors. The total energy density ε is the sum of dynamic, thermal, and magnetic energies:

$$\varepsilon = \frac{1}{2}\rho u^2 + \frac{1}{\gamma - 1} p + \frac{1}{2} B^2, \tag{3}$$

where γ = 5/3 is the adiabatic index, p is the thermal pressure.

[15] For this plasma system, the flux tensor $\mathbf{F}$ in equation (1) is expressed as the following:

$$\mathbf{F} = \begin{pmatrix} \rho\,\mathbf{u} \\ \rho\,\mathbf{u}\,\mathbf{u} + \left(p + \frac{1}{2}B^2\right)\mathbf{I} - \mathbf{B}\mathbf{B} \\ \mathbf{u}\mathbf{B} - \mathbf{B}\mathbf{u} \\ \mathbf{u}\left[\varepsilon + p + \frac{1}{2}B^2\right] - (\mathbf{B}\cdot\mathbf{u})\,\mathbf{B} \end{pmatrix}^T, \tag{4}$$

where I denotes the unit matrix.

[16] The mass loading source vector $\mathbf{P}$ accounts for photo/impact ionization and charge exchange. The major ion and neutral species belong to the water-group. The reaction is simplified to one species of mass m_i = 17 amu. $\mathbf{P}$ can be defined as:

$$\mathbf{P} = \begin{pmatrix} S - L \\ S\mathbf{u}_n - L\mathbf{u} \\ 0 \\ \frac{1}{2}\left(Su_n^2 - Lu^2\right) + \frac{1}{\gamma - 1}\left(\left(\frac{S}{m_i} + f_i n_n\right)kT_n - \frac{L}{m_i}\frac{p}{n_i}\right) \end{pmatrix} \tag{5}$$

where $\mathbf{u}_n$ is the neutral velocity, and the source and loss rates are defined as:

$$S = m_i n_n (f_i + k_{in} n_i) \tag{6}$$

$$L = m_i n_n n_i k_{in}, \tag{7}$$

where $n_i = \rho/m_i$ is the ion number density, n_n is the neutral density, f_i is the total rate of photo and impact ionizations, k_{in} is the ion-neutral charge-exchange rate.

2.2. Inner Boundary at the Body

[17] In our study presented in sections 3.1 and 3.4, Enceladus is modeled as an absorbing body with an insulating surface. The Enceladus surface is considered the inner boundary of the calculation domain. No parameters are simulated inside the body. For this boundary condition, the plasma flow is absorbed as it reaches the surface of the body. On the wake side, the flow is free to leave the body boundary, with a bulk velocity vector equal to the velocity vector of the neighboring flow that is directly downstream of the surface cell. Theoretically the segment of flux rope contains no plasma when it leaves the body, but in MHD a low density (5% of the upstream plasma density) is imposed at the surface to avoid a vacuum wake. Our test indicates that the simulation result is not sensitive to the surface density, unless the surface density is large enough and becomes comparable to the upstream density. The temperature is the body temperature set to 200 K, as suggested by *Hansen et al.* [2008]. The uncertainty of the surface/undersurface temperature of the icy moons is less than 100 K, while our test indicates that our simulation results are not sensitive to temperature variations in this range. The magnetic field is not disturbed at the surface, because for icy moons like Enceladus, Tethys, Rhea and Dione, the con-

Table 2. Parameters Used

Quantity	Symbol	Value
Enceladus radius	R_E	250 km
Gas production rate	Q	$1 \times 10^{28} s^{-1}$
Neutral gas speed	u_n	0.3 km s^{-1}
Ionization rate[a]	f_i	$2 \times 10^{-8} s^{-1}$
Charge exchange rate[b]	k_{in}	$2 \times 10^{-9} cm^3 s^{-1}$
Torus ion number density	n_∞	70 cm^{-3}
Mean ion/neutral mass	m_∞	17 amu
Plasma temperature	T_∞	4×10^5 K
Upstream speed	u_∞	26.4 km/s
Saturn magnetic filed	B_∞	330 nT
Plasma beta	β_∞	0.01
Alfvenic speed	V_A	210 km/s
Sonic speed	V_s	18 km/s
Alfvenic Mach number	M_A	0.1
Sonic Mach number	M_s	1.5
Surface temperature	T_b	200 K

[a]Total of photoionization and electron impact ionization.
[b]From *Huntress* [1977].

ductivity of ice at this temperature is negligible [e.g., *Roussos et al.*, 2008; *Simon et al.*, 2009].

[18] In the simulations for a symmetric mass loading source (see sections 3.2 and 3.3), no body is placed in the domain, so no inner boundary is needed. The obstacle is a mass loading source distributed throughout the entire calculation domain, with a density peak at the origin.

2.3. Neutral Atmosphere

[19] The gravity field of Enceladus is weak, thus the newly released neutrals expand freely into the vacuum to form a supersonic flow (the sonic speed in a 200 K water gas is approximately 280 m/s) with a constant velocity of approximately u_n = 0.3 km/s [*Hansen et al.*, 2006]. In comparison, the escape velocity is about 0.25 km/s at the Enceladus surface, while the radius of the Hill sphere is approximately 4 R_E [*Spahn et al.*, 2006]. Our tests show that the dynamic interaction in the simulation result is not sensitive to the neutral velocity: The result does not exhibit observable differences at the contour levels shown in this paper for hypothetical u_n values ranging from 0.1 to 5.0 km/s. It should be noted that we are assuming the same n_n profile when performing such comparisons. (The linear scaling factors including u_n used in equation (8) should be kept the same). In our MHD model, the distribution of the neutrals is treated as an input background, which is not affected by the plasma distribution.

[20] To simulate the mass loading effect, a neutral density distribution function n_n falling as r^{-2} is adopted:

$$n_n = \frac{Q}{4\pi u_n r^2} \tag{8}$$

where $r = \sqrt{x^2 + y^2 + z^2}$ is the radial distance, Q is the total gas production rate, u_n is the neutral velocity. This distribution assumes constant flux across any closed surface surrounding the origin. In addition, this distribution neglects loss process due to ionization, and neglects particle redistribution due to gravity. Compared with commonly used cometary profiles [e.g., *Hansen et al.*, 2007] that also neglect gravity, this distribution neglects the ionization loss because the ionization scale length is orders of magnitudes larger than the calculation domain.

[21] Such a neutral cloud interacts with the plasma in three ways: photoionization, impact ionization, and charge exchange. The first two increase the total number of ions and electrons, while charge exchange keeps the number and mass of ions constant when transferring the momentum between ions and the neutrals. There are dust particles ejected with the neutrals that become charged [*Jones et al.*, 2009], but these are neglected in our current study. Here we approximate the photoionization and impact ionization as a total electron-creating ionization effect represented by the ionization constant f_i. The ion-neutral charge-exchange rate is treated as a constant, too. The actual impact ionization rate depends on the population of hot electrons, and the charge exchange rate depends on the relative velocity between ions and neutrals. Based on the dissociative recombination rate profile of water group ions [*Jia et al.*, 2007], the probability of recombination is negligible.

2.4. Physical Conditions

[22] Enceladus is located in the inner magnetosphere of Saturn, where the corotating plasma flow is not affected by the solar wind. The upstream number density n_∞, magnetic field magnitude B_∞, flow velocity u_∞ and plasma temperature T_∞ are set to the nominal values, while the total gas production rate Q (used for the symmetric atmosphere) uses the averaged value from previous estimates for the plume [e.g., *Burger et al.*, 2007; *Saur et al.*, 2008], as listed in Table 2. The top and bottom boundaries are fixed with the upstream values to simulate the corotation coupled by the ionosphere, with necessary adjustments according to Saturn's dipole field. The rest boundaries are determined by the values in their upstream adjacent cells. The photoionization and impact ionization rates are simplified into one constant rate. The photoionization rate $f_{ph} = 5 \times 10^{-9} s^{-1}$ is extrapolated from the quiet sun ionization rate at 1 AU [*Huebner et al.*, 1992]. The electron impact ionization process varies with the abundance and temperature of the hot electrons [*Cravens et al.*, 1987; *Tokar et al.*, 2006]. To simplify, a constant of $f_{imp} = 1.5 \times 10^{-8} s^{-1}$ is adopted for this study. The sensitivity of this parameter is discussed in paper 3.

[23] The calculation domain is set to be 80 × 80 × 80 R_E, where R_E = 250 km is the radius of Enceladus. The coordinate system is the ENIS system, where x is along the direction of corotational flow, y is positive toward Saturn, and z is northward [*Dougherty et al.*, 2006]. Multiscale grid [e.g., *Jia et al.*, 2007, Figure 1] is used in this study. The resolution at the moon's surface is 10 km, while the resolution at the boundary is around 80 km. This grid system is designed for all the three papers, to ensure that all necessary signatures regarding the local interactions are included in the calculation domain.

3. Model Results

3.1. Case 1, Pure Absorbing Body

[24] Figure 1 shows the general steady state structures from the simulation result of the interaction between the plasma torus and an absorbing body. The interaction environment around the body is represented by the density,

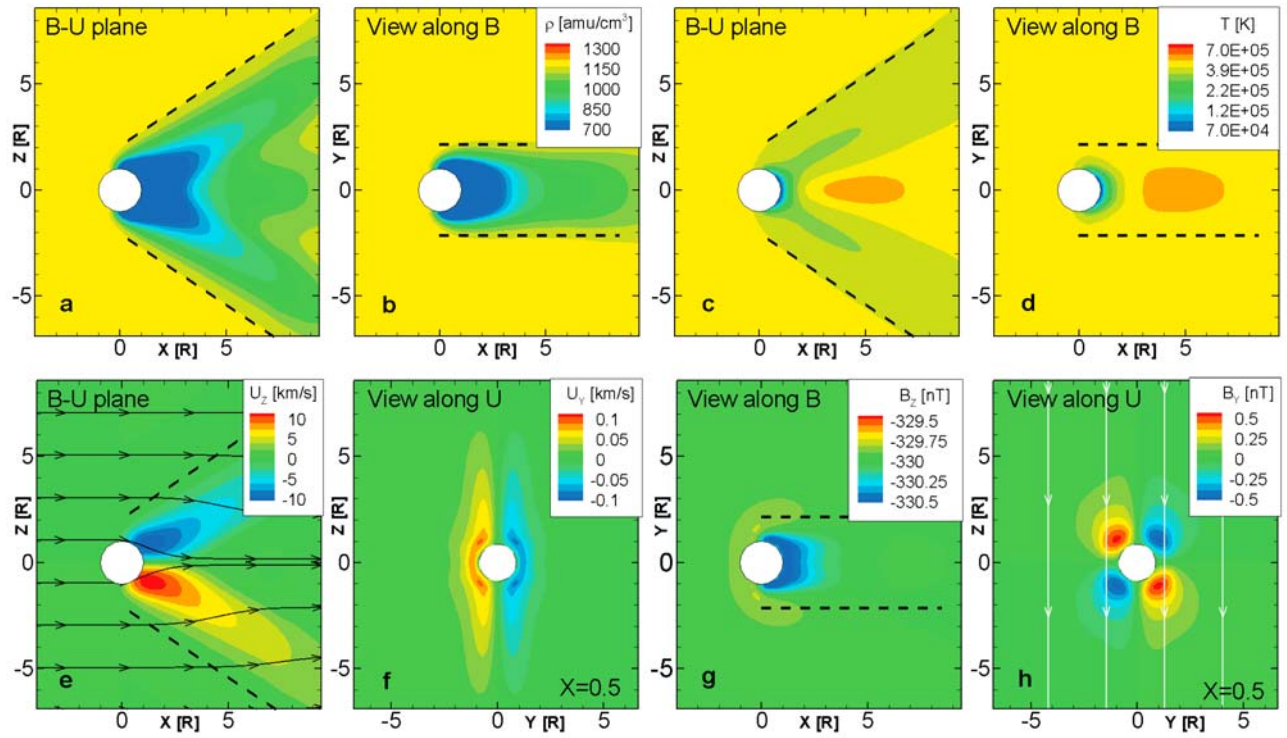

Figure 1. Case 1, torus flow on an absorbing body. (a–d) Density and temperature in the $x - z$ and $x - y$ planes. (e–h) Components of velocity and magnetic field in plane slices. Black lines are stream lines; white lines are magnetic field lines. The planes marked with $x = 0.5$ are slices with constant $x = 0.5$ R_E; others are planes defined by the axes.

temperature, velocity and magnetic field contours. No mass loading is included in this case. The upstream magnetic field is antiparallel to the z axis, while the upstream flow is parallel to the x axis.

[25] In Figures 1a and 1b, density contours are plotted in the $x - z$, and $x - y$ slices. A wake (green and blue regions between the black dashed lines) is created behind the body with a rarefaction wave. The angle of a wake boundary, or the slant angle of the pair of characteristic lines, is determined by the fastest phase speed of the wave perpendicular to the x-directed flow. Figure 2 shows the polar diagram of the phase speed of three MHD waves: fast magnetosonic wave, slow magnetosonic wave and the Alfven wave [e.g., *Benz*, 1993, p. 66]. In this diagram, the sonic speed is an order of magnitude slower than the Alfvenic speed, which is applicable to the fluid condition in this study. The values of the characteristic speeds are listed in Table 2. Since Alfven speed is over 10 times larger than sonic speed, the fast magnetosonic speed $V_f = \sqrt{V_s^2 + V_A^2} = 211$ km/s is very close to the Alfvenic speed 210 km/s.

[26] In case 1, the rarefaction wave propagates parallel to the z axis at the sound speed V_s while the field lines are advected with the x-directed flow at the speed u. These speeds can be estimated with the upstream values: $V_s = 18$ km/s, while $u_\infty = 26.4$ km/s. In the $x - z$ plane (Figure 1a), the angle of the wake boundary (marked with the black dashed lines) is approximately 35°, consistent with the theoretical estimate using the sonic Mach number $M_s = u_\infty/V_s = 1.5 = 1/\tan(35°)$.

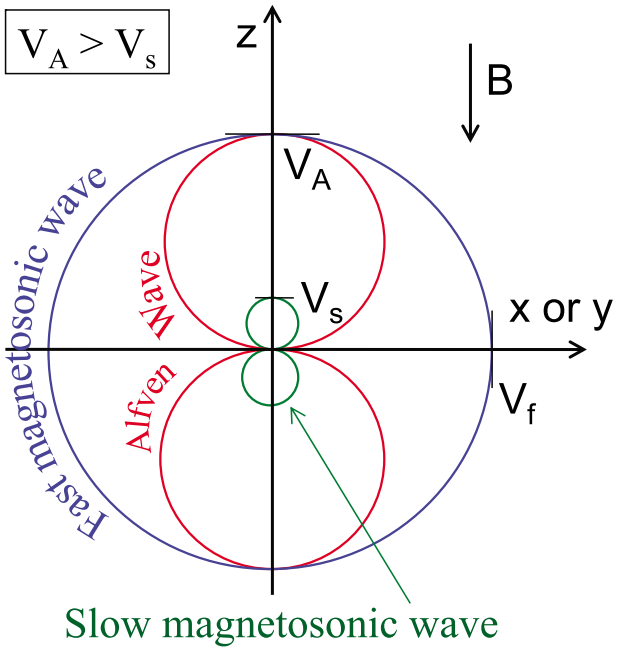

Figure 2. Polar diagram of the phase speed of magnetometric waves when the sound speed is slower than the Alfvenic speed.

[27] In the $x = 0$ plane there are no significant density or pressure disturbances except for those at the surface (not shown). In the $z = 0$ plane (Figure 1b), a density wake can be seen between the two black dashed lines. The density in the wake increases with distance in x due to the filling in along the z direction, as indicated by the thinning blue region. The y extension of the wake is between ± 2 R_E close to Enceladus and kept constant as x increases. Without a background magnetic field, or for a hydrodynamic problem, the solution should be axially symmetric around the x axis. In this case, the strong vertical magnetic field inhibits the density expansion in the y direction. The rarefaction wave travels in the slow mode, which in the cold plasma has zero velocity perpendicular to the field lines.

[28] The temperature profiles are shown in Figures 1c and 1d. In the $y = 0$ plane (Figure 1c), the temperature wake has the same boundary as the density wake, produced by the cooling effect of adiabatic expansion. Close to the surface on the wake side, the temperature decreases sharply where cold ions are released from the surface. In the $z = 0$ plane (Figure 1d), the temperature recovers and increases behind $x = 2$ R_E where kinetic energy (in u_z) is converted into thermal energy.

[29] There is no significant u_x or B_x perturbation in either of the three planes (u_x is shown in Figures 8c and 9c; others not shown). For such an absorbing body, there is no slowdown of the flow to create a nontrivial B_x component, because the plasma flowing into the body is absorbed without any resulting disturbance.

[30] Figures 1e and 1f show u_z and u_y contours with black stream lines. There is no significant perturbation of u_z in the $x = 0$ and $z = 0$ planes (not shown). The u_z acceleration in the $y = 0$ plane (Figure 1e) is due to the low pressure in the rarefaction wake. At the x axis, the flows originating from the $+z$ and $-z$ regions (blue and red, respectively) collide and transfer their kinetic energy into thermal energy. (This conversion is the solution when an isotropic Maxwellian distribution is imposed in MHD. More accurate study of the wake requires the consideration of anisotropic pressure.) Consequently, in Figures 1c and 1d, there is a hotter island of plasma along the x axis in the region downstream of the u_z perturbations. Our tests show that this u_z is dependent on the plasma temperature and surface density on the wake side: For a hypothetical surface temperature an order of magnitude higher, the wake becomes about 1% shorter while u_z becomes 1% stronger because the hotter plasma refills faster. For a surface density equal to the upstream plasma density, the wake nearly disappears because now the thermal pressure gradient is caused only by the temperature difference.

[31] There is no significant u_y perturbation in the $x - z$ or $x - y$ planes. Shown in Figure 1f is a slice with constant $x = 0.5$ R_E, which is slightly downstream. The u_y perturbation is two orders of magnitude smaller than that of u_z, because it is harder to bend the strong magnetic field lines than to create a flow parallel to these lines. The two orders of magnitude difference is consistent with the plasma β of 0.01.

[32] Figures 1g and 1h show the B_z and B_y perturbations caused by the Enceladus body passing through the plasma. In the wake shown in the $x - y$ plane (Figure 1g), the magnitude of B_z decreases by 0.1% in the flanks and increases by 0.3% close to the surface. The decrease and increase of the magnetic field is the result of the perturbation in the thermal pressure. In the wake where thermal pressure is significantly decreased, the field increases, and in the flanks, the field decreases to conserve the divergence of B.

[33] The 0.1% decrease in front of the body is the effect of the decrease in the flanks because the flow is subsonic. This small decrease and increase is driven by the small y component of the velocity. We note that in the y direction, which is perpendicular to the magnetic field, the field perturbation propagates with the fast mode velocity V_f.

[34] In the $y - z$ slice at $x = 0.5$ R_E (Figure 1h), there is <0.5 nT B_y perturbation, indicating the field lines bend toward the x axis (note that the main field is in the $-z$ direction), which is consistent with the rarefaction and compression in B_z. Again this field perturbation does not show a strong $y - z$ asymmetry, because the fast magnetosonic speed is similar along the y and z directions. The perturbations in the magnetic field in the wake close to the body are consistent with the sketch by *Spreiter and Alksne* [1970, Figure 16] and with the Cassini magnetometer observations at Tethys and Rhea, the two icy moons with no or weak mass loading [*Khurana et al.*, 2008]. The shape of the flow perturbation in the $y = 0$ plane is also comparable to the recent hybrid simulation results of Rhea [*Roussos et al.*, 2008] and Tethys [*Simon et al.*, 2009] in cold plasma. In the $z = 0$ plane, ideal MHD does not include the gyroradius effect so there is no asymmetry as shown in the hybrid results. In addition, single fluid MHD assumes Maxwellian distribution so there are no counterstreaming particles in the wake in this simulation, to be compared directly with Figure 3 by *Khurana et al.* [2008] and Figure 4 by *Simon et al.* [2009].

[35] In summary, an absorbing body in such a submagnetosonic torus flow creates a density wake with increased temperature and limited magnetic perturbations. The solution space is separated by a characteristic surface. The angle between the x axis and the surface varies in different directions. In its intersection with the $y = 0$ plane, the angle is defined by the ratio between the fast magnetosonic speed and the flow speed. Similarly, the angle in the $z = 0$ plane is defined by the ratio between the slow magnetosonic speed and the flow speed. Although the flow field is submagnetosonic, the perturbation that propagates upstream is insignificant: with the set of contour levels shown here, only in Figure 1g can we identify an upstream perturbation, whose magnitude is barely 0.1% of the background value. Consequently, the flow field upstream of the expansion Mach cone appears to be undisturbed, because the density rarefaction tends to propagate in the slow mode, whose speed is zero across the field lines.

[36] In their review paper, *Spreiter and Alksne* [1970] illustrated the perturbation by such an absorbing body in a supersonic flow using convected-field gasdynamic simulations. *Lipatov et al.* [2002] and *Hansen et al.* [2007] presented 3-D hybrid simulations on the interaction between solar wind and weak comets as absorbing bodies with limited mass loading. Compared with our subsonic case, the geometry of the dynamic perturbations close to the body is similar, except for the following differences: the angles of the Mach cones are different; there is a trailing shock in the supersonic case while there is no shock in the subsonic case; and the small magnetic perturbation does not propagate

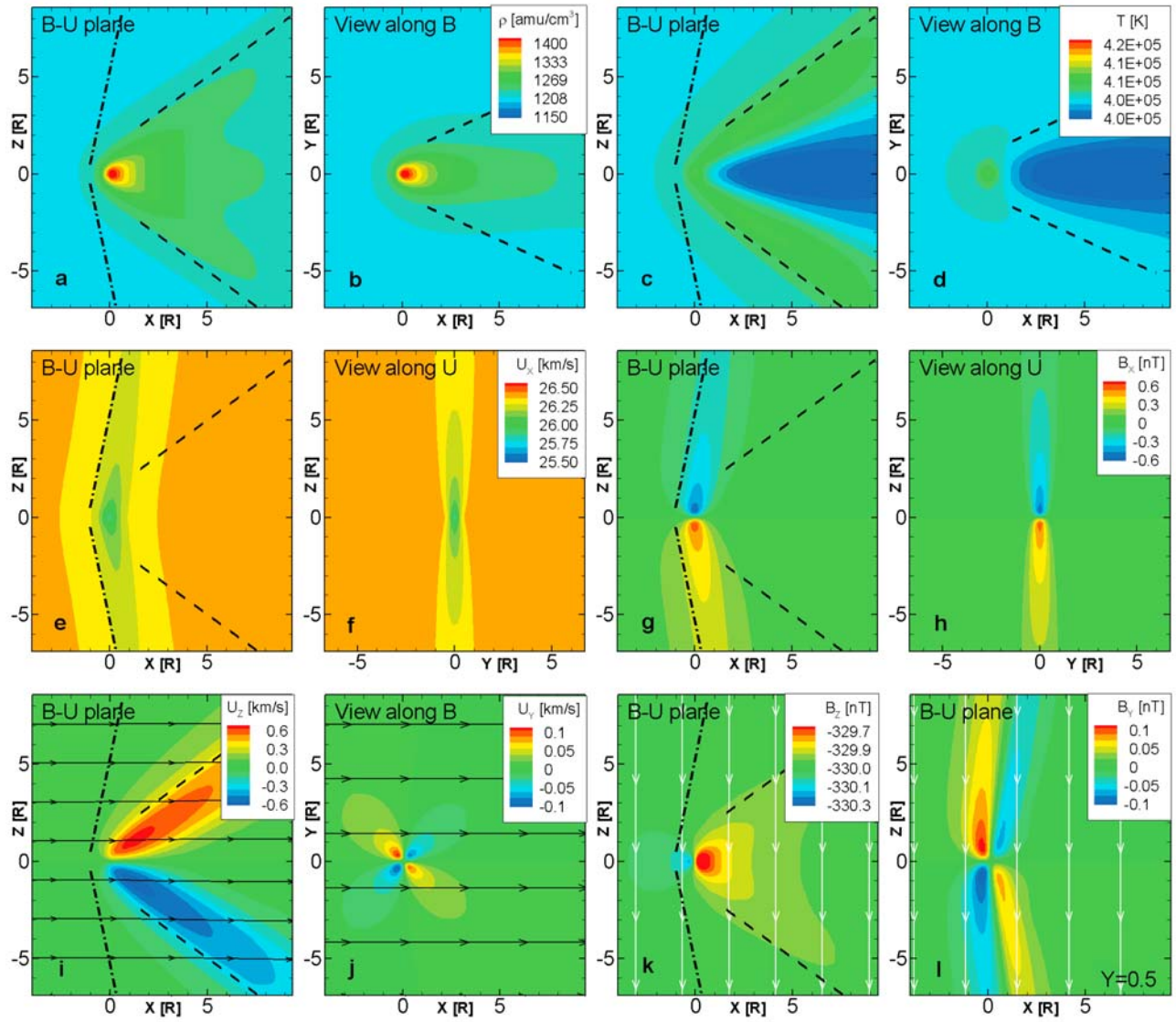

Figure 3. Case 2, torus flow on a neutral cloud that is ionized by photons and hot electrons. (a–d) Density and temperature in the $x - z$ and $x - y$ planes. (e–h) The u_x and B_x contours. (i–l) Values of u_y, u_z, B_y, and B_z in plane slices. Figures 3i–3l show thermal and magnetic pressures. All slices are in the plane containing the origin. Black lines are stream lines; white lines are magnetic field lines.

upstream in the supersonic case while it does in the subsonic case here.

[37] The interaction of plasma flow with nonconducting, nonmagnetic moons is studied by recent hybrid and full particle models [e.g., *Birch and Chapman*, 2001; *Kallio*, 2005; *Simon et al.*, 2009]. Our current MHD model forces Maxwellian distribution in the calculation, so it is necessary to adopt kinetic effects such as anisotropic pressure terms in future studies to observe the fine structures created by the plasma-moon interaction more accurately.

3.2. Case 2, Spherically Symmetric Electron-Creating Ionization Source

[38] Before we move to a complete mass loading simulation, we quantify the total of photo and impact ionization effects in case 2. In contrast to case 1, there is no physical body representing Enceladus. The obstacle to the upstream torus plasma is due to the ion pickup caused by such electron-creating ionizations from the neutrals distributed, as in equation (8).

[39] Figure 3 shows our 3-D simulation result. In Figures 3a and 3b, density contours are plotted in the $y = 0$ and $z = 0$ slices. There is no obvious density increase following the dash-dotted lines, because the density increase caused by the slowed flow is weaker than the local pickup. The density increases in the cone between the pair of dashed lines, with an angle of approximately 35°, similar to the wake angle in case 1. This angle is created by a pair of rarefaction waves propagating from the high-density regions caused by pickup. In the $z = 0$ plane (Figure 3b) this density tail slightly decreases its width with x distance because of diffusion. Compared with case 1 (also see Figures 8a, 8e, 9a, and 9e), this obstacle results in a pure density increase centered at the density peak of the neutrals.

[40] Figures 3c and 3d show the temperature contours in the $y = 0$ and $z = 0$ planes. The temperature in the expansion fan increases because of the pickup and then decreases close to the $+x$ axis because of the combination of two processes. On average, a newly picked up ion is traveling at velocity $\mathbf{v} = \mathbf{u} + \mathbf{v}_{Tn}$ relative to the plasma, where $v_{Tn} \approx 0.3$ km/s is the thermal velocity of the neutrals (negligible compared to the flow velocity u). The new ion is then accelerated to the bulk flow speed. In the inertial frame, this acceleration process transfers kinetic energy from the bulk flow to the new ion. In the observing frame that moves with the flow, kinetic energy is taken from the particle to heat the flow. This relative velocity converts to a thermal energy of 57 eV, higher than the plasma temperature 40 eV. Thus pickup causes a temperature increase (see the first term on the right-hand side of equation (8)). Alternatively, there is a pressure gradient in the wake region, pointing in the $+x$ direction. This pressure causes an adiabatic expansion toward the $-x$ direction that results in a temperature decrease. In Figure 3d, the region of temperature decrease slowly expands with an angle close to 35°. Again, there is no obvious temperature increase along the Alfven wings. The peak temperature is located at the origin, with a less than 2% increase above the torus value. For the reader's convenience, the original form of the energy equation is listed below, which is equivalent to its conservative form as listed in equations (1)–(7):

$$\frac{1}{\gamma-1}\frac{\partial p}{\partial t} + \frac{1}{\gamma-1}(\mathbf{u}\cdot\nabla)p + \frac{\gamma}{\gamma-1}p(\nabla\cdot\mathbf{u}) = \frac{1}{2}S(\mathbf{u}_n - \mathbf{u})^2 + \frac{kT_n}{\gamma-1}\left(\frac{S}{m_i} + n_n f_i\right) - \frac{1}{\gamma-1}\frac{L}{m_i}\frac{p_i}{n_i}, \quad (9)$$

where $p_i = p/2$ is the ion pressure, and the extra $n_n f_i$ term comes from the energy of electrons created by photo/impact ionization processes. It should also be noted that the illustrated effects are dominant for such cases with low gas production rate and low ionization rate. For cases with gas density or ionization rate orders of magnitudes higher, such as the interaction around an active comet, the relative speed decreases significantly close to the mass loading center from the background value and thus this energy transfer process works differently. As an example, a subcase with 10 times the current photo/impact ionization rate creates a temperature decrease after the center, which is close to the contact surface around an active comet [see *Jia et al.*, 2007, Figure 2]. More details are discussed in case 3.

[41] Shown in Figures 3e and 3f are the u_x velocity contours. The green color indicates a slight (<2%) slowdown of the torus flow. This perturbation propagates in the $\pm z$ direction (along the background field) with the fast magnetosonic speed, which equals the Alfven speed: V_A = 210 km/s. The angle between the x axis and the dash-dotted lines is 83°, consistent with the estimate using the fast magnetosonic Mach number $M_f = M_A = u/V_A = 0.12 = 1/\tan(83°)$ (see Table 2). Such a slowing down forms an Alfven wing system [*Neubauer*, 1980] as a result of the mass increase in the flux tubes, when newborn ions are picked up by the frozen-in magnetic field. Although its magnitude is decreasing away from the $z = 0$ plane, this u_x perturbation extends to near the top and bottom boundaries. In the y direction, the u_x gradient is sharper and stays within about 1 R_E because the magnetic field is mainly in the z direction (Figure 3f).

[42] Figure 3g shows the B_x contours in the $y = 0$ plane. The B_x perturbation is <0.2% of the field magnitude, while the shape of the perturbation is consistent with that of the u_x contours. The u_x slowdown creates the B_x perturbations, while the maximum density variation in the density wings depends on the point source's intensity. At its minimum, u_x drops to 94% of its background value. When the gas production rate (Q) increases, the mass loading increases at each point in the calculation domain, as can be seen from the neutral density equation (equation (8)), and thus the flow is slowed down more effectively.

[43] Figure 3h shows the B_x contours in the $x = 0$ plane. As can be inferred from Figures 3g and 3h, there is no significant B_x perturbation in the $z = 0$ plane. In the $x = 0$ plane, the u_x gradient in the y direction is sharper than in the z direction because the magnetic field is mainly in the z direction (Figure 3f). The slant angles between the x axis and the contour level boundaries are determined by two major factors: the angle (75°~85°) close to the mass loading center is defined by the ratio between the Alfven speed and the local sonic speed. The x tilt of the Alfven wings results in faster decrease of B_x perturbation than that shown in Figure 3g. In the $z = 0$ plane, the u_x perturbation propagates both upstream and downstream in bent characteristic lines. This is not directly shown but can be indicated by comparing Figures 9g and 9k). Our tests show that by changing the minimum and maximum contour levels in Figure 3g to 25.72 and 26.595, respectively, Figure 3g can appear similar to Figure 3k. Alternatively, as can be inferred from the B_x plots (Figures 3g and 3h), there is no significant B_x perturbation in the $z = 0$ plane.

[44] Because of the symmetry of this interaction, there is no significant u_y perturbation in the $y = 0$ plane, or significant u_z perturbation in the $z = 0$ plane. The u_z contours in the $y = 0$ plane and u_y contours in the $z = 0$ plane are shown in Figures 3i and 3j. In the $x - z$ plane, a large u_z is created, pointing away from the obstacle, coincident with the density expansion fan. Compared with the case 1 result, the expansion angle is similar, but the red-blue colored region is reversed. In the $x - y$ plane, the u_y contours show a symmetric deflection around the obstacle. The perturbations in u_z and u_y are <3% of the magnitude of the flow speed.

[45] The B_z perturbation in the $y = 0$ plane is shown in Figure 3k. The white lines are projected magnetic field lines. On the upstream side of the body, the total field increases (blue), while along the z axis and in the wake, the total field decreases (red, yellow and light green). The magnetic field perturbation on the downstream side roughly follows the profile of the expansion cone. The B_y perturbation in the y = 0.5 R_E plane is shown in Figure 3l. There is no significant B_y perturbation in the $y = 0$ or $z = 0$ planes because of the symmetry. Upstream of the origin in this y = 0.5 R_E plane, the field bends away from the $y = 0$ plane in the northern part but toward the $y = 0$ plane in the southern part. At the down stream side, the B_y distribution is reversed. This B_y perturbation is the result of the Alfven wing current system [e.g., *Russell and Huddleston*, 2000, and references therein]. Close to the y axis with $y > 0$, there is a pair of field line currents that direct to the mass loading center (not shown in this paper). Around the mass loading center the current flows in the $-y$ direction as the result of motion electric field that is caused by the slowing down flow. On the $y < 0$ side

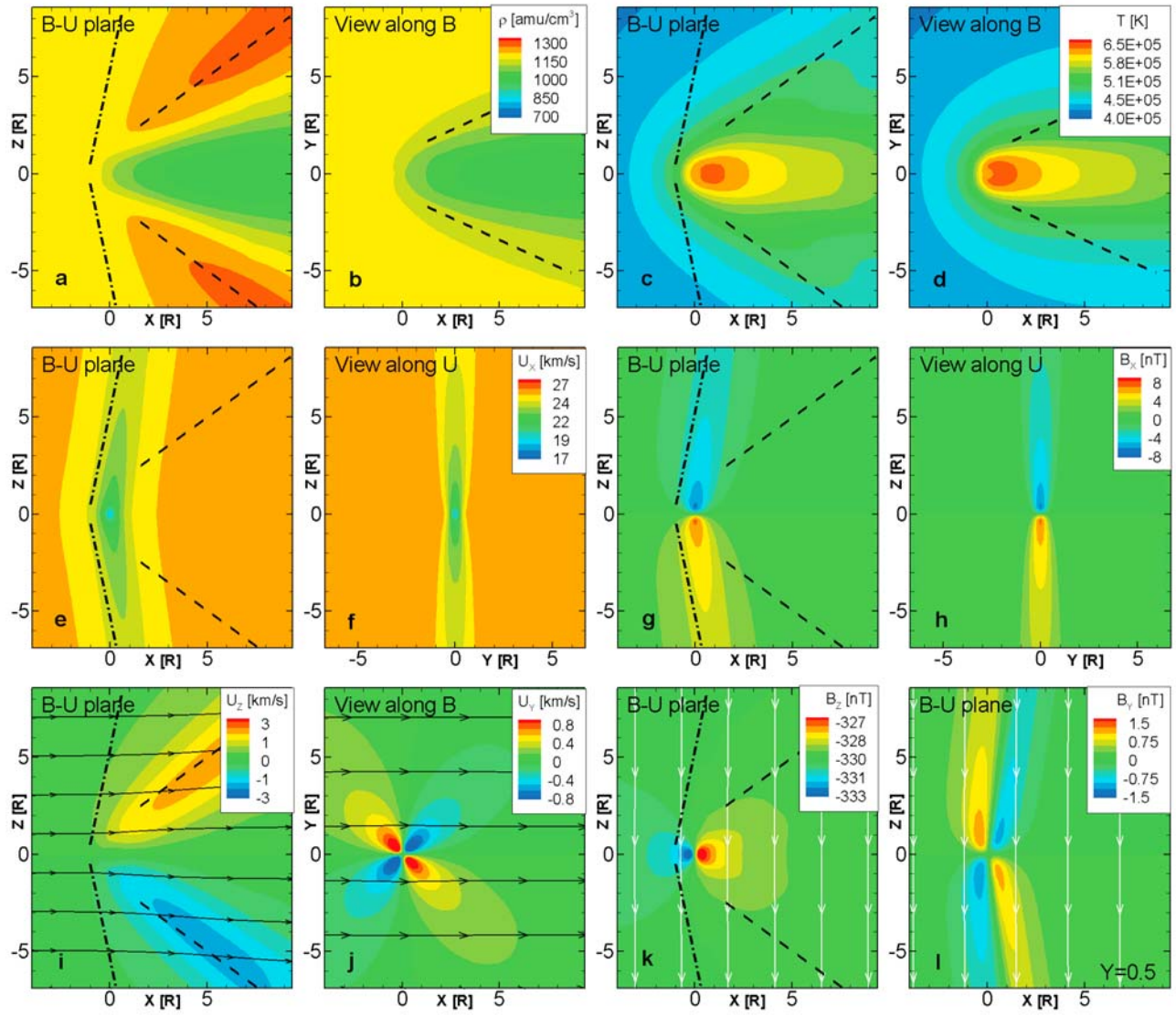

Figure 4. Case 3, torus flow on a charge-exchanging neutral cloud. Contours of density, temperature, velocity, and magnetic field components are shown in plane slices. Black lines are stream lines; white lines are magnetic field lines. The plane (Figure 4l) marked with $Y = 0.5$ is a slice with constant $Y = 0.5$ R_E; others are planes defined by the axes.

the current flows away from the mass loading center to the ionosphere.

[46] In summary, a spherically symmetric photo/impact ionization source creates a density increase that effectively slows down and deflects the torus flow proportionally to the strength of the photo/impact ionization source. The magnetic field lines drape around the source center and display B_y perturbations whose signs are opposite to that of an absorbing obstacle.

3.3. Case 3, Spherically Symmetric Charge Exchange Source

[47] Based on the same neutral density distribution used in case 2, in case 3 we model the effect of charge exchange from the same neutral cloud. Again, in this case there is no physical body representing Enceladus. The model results are shown as 2-D contour plots in Figure 4.

[48] Figures 4a and 4b show the density contours in the $x - z$ and $x - y$ plane. The maximum density variation is less than ±20%. In contrast to case 2, there is no density peak around the point source. Rather the density increases downstream of the Alfven wings, marked by the dash-dotted lines with an angle of approximately 83°, as the same result of velocity decrease as case 2. In both flanks the angles of the dashed lines to the ram direction are 35°. Downstream of these lines, the density peaks and starts to decrease, caused by the expansion behind the deflected flow around the point source. The angle of this expansion fan is similar to that of case 1, which is also determined by the upstream sonic Mach number. Downstream of the mass loading center along the x axis, the reaccelerating flow between the two expansion fans causes a density decrease.

[49] In Figure 4b, the density also decreases between the pair of dashed lines due to the speedup of the local flow. In

contrast to the rarefaction tail with slightly decreasing width away from the origin in case 1, this tail in case 3 increases its width (also see Figures 9a and 9i), indicating the outward deflection of the plasma in the y direction, as can be seen in the stream lines and u_y plots in the $z = 0$ slice of Figure 4j.

[50] Figures 4c and 4d show the temperature contours in the $y = 0$ and $z = 0$ plane. The boundary of the tail in the $y = 0$ plane (green region in Figure 4c) is similar to the peak of the density compression region (red region) shown in Figure 4a. The maximum temperature increase is about 50% of the torus value. In the wake, in contrast to case 2's results that show a decreased temperature by 2%, the temperature from case 3's result shows a 60% maximum increase from the background. This is a combination of five processes: in addition to the pickup heating and expansion cooling that happen in case 2, the folding flow in the z direction (as shown in Figure 4i) causes a temperature increase, similar to the heating in the wake of the case 1 result. The fourth effect is caused by the sharp decrease in flow velocity across the Alfven wings. At the mass loading center, the velocity decreases to below 20 km/s, which corresponds to a pickup energy comparable to 40 eV (21 km/s). This rapid decrease in pickup energy causes a slight temperature decrease near the neutral source center. The fifth process is the removal of thermal energy by the old ions that now become neutrals. This process by itself removes ion density too, so its effect is not as obvious as the pickup and dynamic processes. In general the pickup heating and folding flow heating are the two dominant processes that result in an overall increased temperature. The only exception is at the mass loading center where the flow velocity is below 20 km/s, thus the pickup process does not cause heating.

[51] The background flow is slowed down due to momentum exchange between ions and neutrals, as shown in Figures 4e and 4f. In theory, because the torus flow speed is slower than the fast magnetosonic speed, the steady state perturbation to the flow extends from $x = -\infty$ to $x = +\infty$ along the x axis. In the $x - z$ plane (Figures 4e and 4g), the Alfven wing structure can be seen from the u_x contours (Figure 4e) and the B_x contours (Figure 4g). The angle of the Alfven wings is consistent with the density wings marked by the dash-dotted line in Figure 4a. Such a slowdown creates the B_x perturbations, while the maximum density variation in the density wings depends on the intensity of the point source. The minimum u_x drops to 60% of the background value.

[52] In the y direction, the u_x gradient is sharper, with a shape comparable to the case 2 result (Figures 3f and 4f). In the $z = 0$ plane (Figure 9k), the u_x perturbation propagates both upstream and downstream along bent characteristic lines due to the modification to the ambient flow condition by mass loading. These angles can be roughly averaged to 35° upstream and 30° downstream due to the temperature difference. Moreover, as can be inferred from the B_x plots (Figures 4g and 4h), there is no significant B_x perturbation in the $z = 0$ plane.

[53] In comparison with the case 2 result, Figures 4e, 4f, 4g and 4h show the same shape while the perturbation is an order of magnitude stronger. The difference in the perturbation is not only due to the different mechanism of mass loading, but mainly due to the difference in the reaction rates. The chance for each neutral particle to be ionized via photo/impact ionization is approximately 2×10^{-8} s^{-1}, while the chance of ionization via charge exchanging with an ion is $n_i k_{in} \approx 70 \times 10^6$ m^{-3} $\times$ 2×10^{-15} m^{3}s^{-1} $= 1.4 \times 10^{-7}$ s^{-1}, which is an order of magnitude larger than the former. In addition, the charge-exchange rate is estimated using the torus ion density. The ion density increases close to the mass loading center, so the ratio between real charge-exchange rate versus photo/impact ionization rate is even larger than the estimated value (except in the body wake discussed in case 4).

[54] The density profile is also consistent with the u_z and u_y plots in Figures 4i and 4j. There is no significant u_z perturbation in the $z = 0$, $x = 0$ planes (not shown). In the $y = 0$ plane (Figure 4i), the u_z contours show an expansion wave with an angle of approximately 35° in the z direction, which is consistent with the density wake in Figure 4a. The plasma close to this plane is deflected along the z axis in front of the mass loading center. Across the expansion fans, the plasma is deflected again toward the x axis. These deflections are driven by the thermal pressure distribution (not shown). On the other hand, there is no significant u_y perturbation in the $y = 0$ plane (not shown here). In the $z = 0$ plane (Figure 4j), the u_y contours show a deflection around the mass loading center. In a $x - z$ cut with $y = 0.5$ R_E, this deflection propagates in the z direction with the Alfven speed (not shown). The u_y distribution can be indicated from the B_y contour shown in Figure 4l. As obstacles that deflect the flow around themselves, the source in case 3 results in a distribution of u_y that is similar to that of the case 2 result.

[55] Figures 4k and 4l show the B_z and B_y contours in two $x - z$ planes with $y = 0$ and $y = 0.5$ R_E, respectively. The maximum B_z perturbation is below 2% at this resolution. It should be noted that the neutral density at the origin is mathematically infinity, so higher resolution close to the origin results in an artificial singular point, which is beyond the scope of this study. Our tests (not shown here) indicate that higher resolution in this region results in a sharper gradient in the B_z perturbation at the origin. The current result physically limits the peak neutral density at the origin, which is closer to reality.

[56] At the upstream side the field piles up, so the field strength increases (blue), while in the tail side the field straightens to "catch up" with the background field, and the field strength decreases (red). The B_z contours in the $z = 0$ plane (not shown) appear close to that in the $y = 0$ plane, except for the former appearing thinner in the tail. At the downstream side the field still convects slower than the background, and y dimension convection is also involved. Thus a lower density region is associated with the field decrease (Figures 4a and 4b). Compared with Figure 4e, it should also be noted that although the bent field lines in the $y = 0$ plane straighten to "catch up" with the corotational speed in the top and bottom boundaries (simulating the rigid rotation in the Saturn ionosphere), u_x never becomes larger than the corotating speed. This is because along the $+x$ axis, the increase of B_z to its background value (between $0 < x < 5$ R_E) is mainly due to the flux carried by the flow in the y direction from both flanks, instead of a pure x direction "catch-up" of flux tubes.

[57] Due to the symmetry of this interaction, there is no significant B_y perturbation in the $y = 0$ or $z = 0$ planes (not

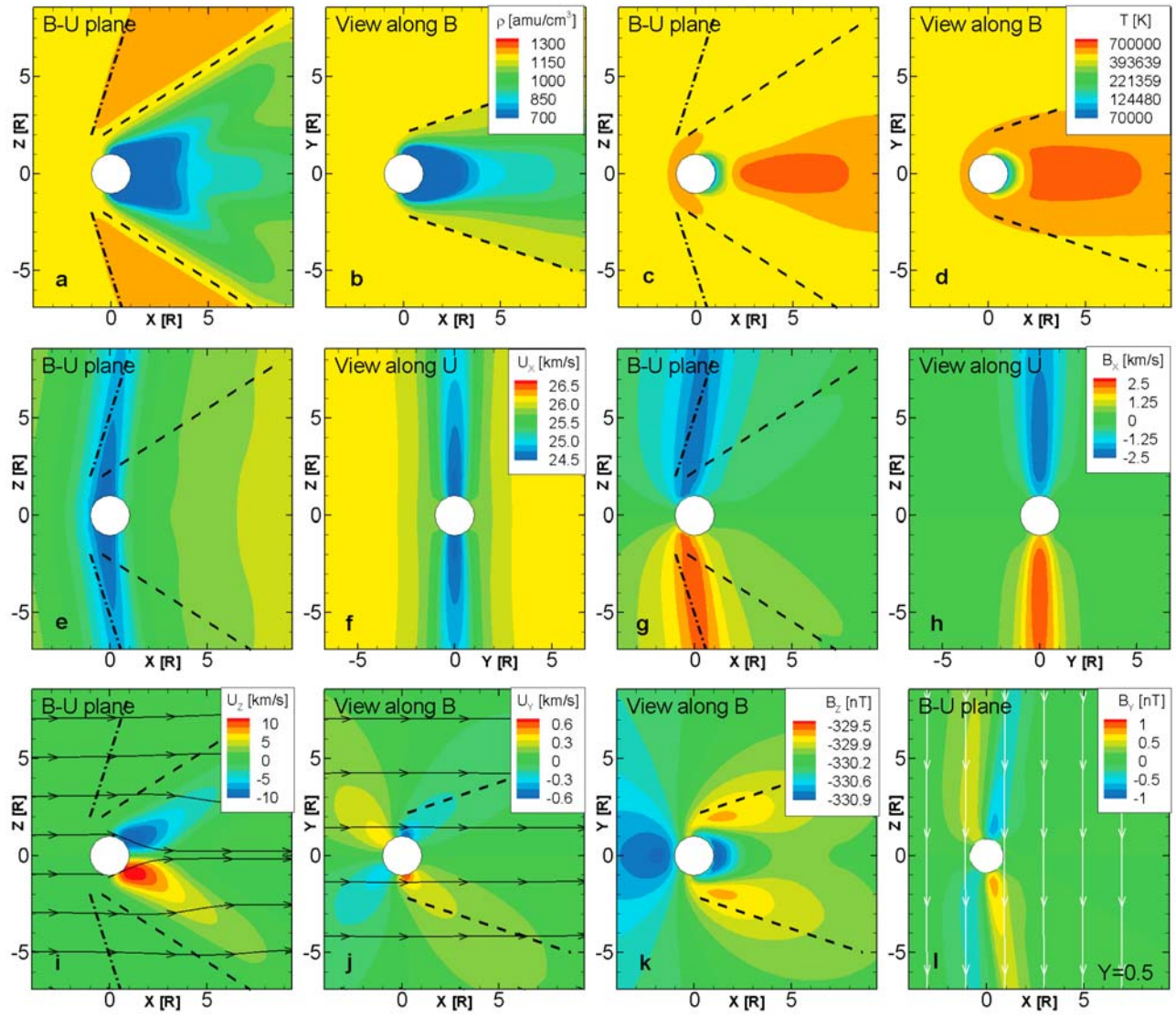

Figure 5. Case 4, torus flow into a mass-loading region centered on an absorbing body. Contours of density, temperature, velocity, and magnetic field components are shown in plane slices. Black lines are stream lines; white lines are magnetic field lines. The plane (Figure 5l) marked with $Y = 0.5$ is a slice with constant $Y = 0.5$ R_E; others are planes defined by the axes.

shown). Figure 4l shows the $x - z$ cut with $y = 0.5$ R_E. At this flank of the point source, the B_y perturbation exhibits outward bending at the upstream side with inward bending at the tail side. Such bending propagates in the z direction to a large distance in the Alfven speed.

[58] In summary, the flow and field perturbation of case 3 (charge exchange) has a similar shape to that of case 2 (photo/impact ionization), which is an order of magnitude weaker in intensity. The density and temperature distributions are different, revealing the physical difference between these two mass loading processes. Photo and impact ionization increases the plasma flux while charge exchange keeps the flux constant. Both processes create cool newly born ions that decrease the total plasma thermal energy. Both processes slow down and deflect the upstream flow so that the density and temperature tend to increase (in different regions). On the other hand, the mass loading cases (cases 2 and 3) are fundamentally different from case 1 (absorbing body), not only because of the mass addition itself, but also because the distribution of the mass loading in the entire simulation domain. Although the slow mode waves cannot propagate upstream, the local pickup already disturbs the upstream flow, creating a slightly modified flow field from the far torus value. Such a mass loading source interacting with a supersonic flow is widely studied by cometary MHD simulations, as reviewed by *Cravens and Gombosi* [2004], which is significantly different from this case.

3.4. Case 4, Absorbing Body and Mass Loading

[59] In case 4, we model the combined effect of an absorbing body and a spherically symmetric mass loading source in an incident plasma flow, as a combination of cases 1, 2 and 3. In this case, the neutral distribution serves as an

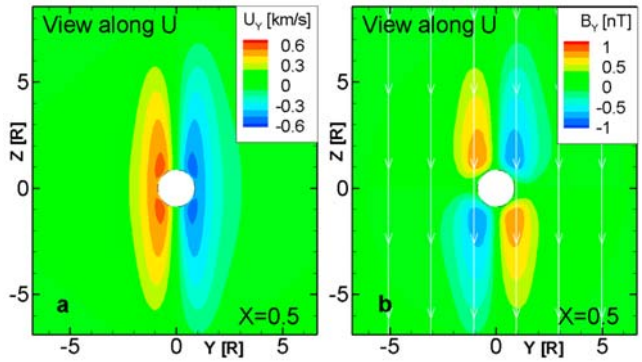

Figure 6. Case 4, contours of velocity and magnetic field y components in the x = 0.5 R_E plane, for comparison with Figure 1. White lines are magnetic field lines.

atmosphere of the absorbing moon. The model results are shown as 2-D contour plots in Figure 5.

[60] Figures 5a and 5b show the density contours in the $x-z$ and $x-y$ plane. In the $y = 0$ plane (Figure 5a), a density pileup is formed in the z direction between the black dash-dotted lines, which is consistent with the Alfven wings in Figure 5e and comparable to the pileup in case 3 result (Figure 4a). A rarefaction wake between the dashed lines is formed, which is comparable to that of case 1 (Figure 1a) and which dominates over the effect of u_z in case 3 (also see Figures 8a, 8i and 8m). In the $z = 0$ plane (Figure 5b), the wake shows both broadening (marked by the dashed lines) and thinning in different contour levels along the x axis, which are comparable to case 3 and case 1, respectively (also see Figures 9a, 9i and 9m).

[61] Figures 5c and 5d show the temperature contours in the $y = 0$ and $z = 0$ planes. Compared with the case 1 result, which is shown with contour levels similar to the case 4 result, the temperature decreases less in the rarefaction wake and increases more around the x axis (also see Figures 8b, 8n, 9b and 9n).

[62] The background flow is slowed due to momentum exchange between ions and neutrals, as shown in Figures 5e and 5f. Because the density at the body surface is lower than the density at the origin of the point source, the flow is slowed less than in case 3 (also see Figures 8k, 8o, 9k and 9o). With fine resolution in contour levels, we can see that the mass loading effect decreases u_x (by less than 1%) throughout the plotted area. Consequently, a B_x component is created, as shown in Figures 5g and 5h. In general, the u_x and B_x contours exhibit similar shape as in case 3, although the magnitude of perturbation is smaller: e.g., at (0,0,2) R_E, the case 3 perturbation is 1.7 times the case 4 perturbation to u_x. This indicates that although case 4 has combined the effects of all three chemical reactions, the momentum loss at the mass loading center is still strong enough to cause significant deceleration at locations along the field lines, such as at this point.

[63] The u_z and u_y contours are plotted in Figures 5i, 5j and Figure 6a. In the $y = 0$ plane (Figure 5i), the u_z contours appear similar to the case 1 result (also see Figures 8d and 8p), due to the strength of u_z caused by the density wake behind the body. Compared to case 3, the deflection of u_z can be seen from the curvature of stream lines, but is not obvious in the contour plots. This is consistent with the density contour in Figures 5a–5d. In the $z = 0$ plane (Figure 5j), u_y shows a deflection around the body, with a magnitude over 20 times smaller than the peak u_z. These u_y contours are comparable to those of case 3, indicating that the absorbing body does not significantly affect the deflection of the flow (also see Figures 9l and 9p). In the x = 0.5 R_E plane (Figure 6a), u_y shows bending toward the x axis, which is comparable to the case 1 result but 6 times stronger. This is not directly comparable with the mass loading "dominant" case by *Khurana et al.* [2008, Figure 10], which exaggerates the effect of the ionosphere by intense mass loading.

[64] Figures 5k and 5l show the B_z and B_y contours in the $x-y$ and $y-z$ planes. The maximum B_z increase is less than 0.3%, while the decrease is less than 0.2%. Similar to case 3, the field piles up on the upstream side so the field strength increases (blue). However, on the downstream side, the density wake causes the flow to fold toward the x axis from the y direction, causing the field to increase at the x axis while decreasing in the flanks, which is comparable to that of case 1. In the B_y contours in the $x-z$ plane at constant y = 0.5 R_E, the profile is similar to the case 3 result while the intensity is only half as large. Figure 6b shows the B_y perturbation in the x = 0.5 R_E plane to compare directly with the case 1 result. The directions of $\triangle B_y$ are distributed similarly while the intensity created by case 4 is twice as strong. This is because the deflection of the decelerating flux ropes in front of the mass loading moon further decreases the magnetic pressure in the wake.

[65] Two subcases are studied but not shown here. Our tests indicate that the combination of photo/impact ionization with the absorbing body, and the combination of change-exchanging atmosphere with the absorbing body result in comparable perturbations to the interaction region. For the photo/impact ionization with body case, the effect of mass loading is also much weaker, so the result is dominated by the type of interaction closer to the absorbing body case.

[66] In another two subcases, the location of the mass loading center is shifted in the $-z$ direction, as shown in Figure 7. The differences in neutral density are shown in Figures 7e and 7i. The original case 4 results are shown in Figures 7a, 7b, 7c and 7d. The first subcase place the neutral density peak at the south pole of the moon, while the second one place the neutral density peak at -3 R_E. Such a displacement moves the resulting peak ion density in the $-z$ direction, so the interaction region becomes asymmetric about the $z = 0$ plane, compared with the case 4 result.

[67] Comparing Figure 7b with Figures 7f and 7j, the displaced mass loading center results in an equally displaced density peak. The characteristic lines are modified accordingly. Figures 7g and 7k show the resulting Alfven wings with the u_x component of velocity. The northern wings are thinner than the southern wings in this plane. In the $x = 0$ plane (not shown), we found the northern wings wider than the southern wings. In Figure 7h and 7l, the pair of increase/decrease perturbations in B_z is shifted with the neutral density peak, while a new decrease/increase pair is seen in the corotational wake of the moon. This pair appears only when there is a displacement between the mass loading center and the moon center, which is true for Enceladus. The magnitude of perturbation of this pair is an order of mag-

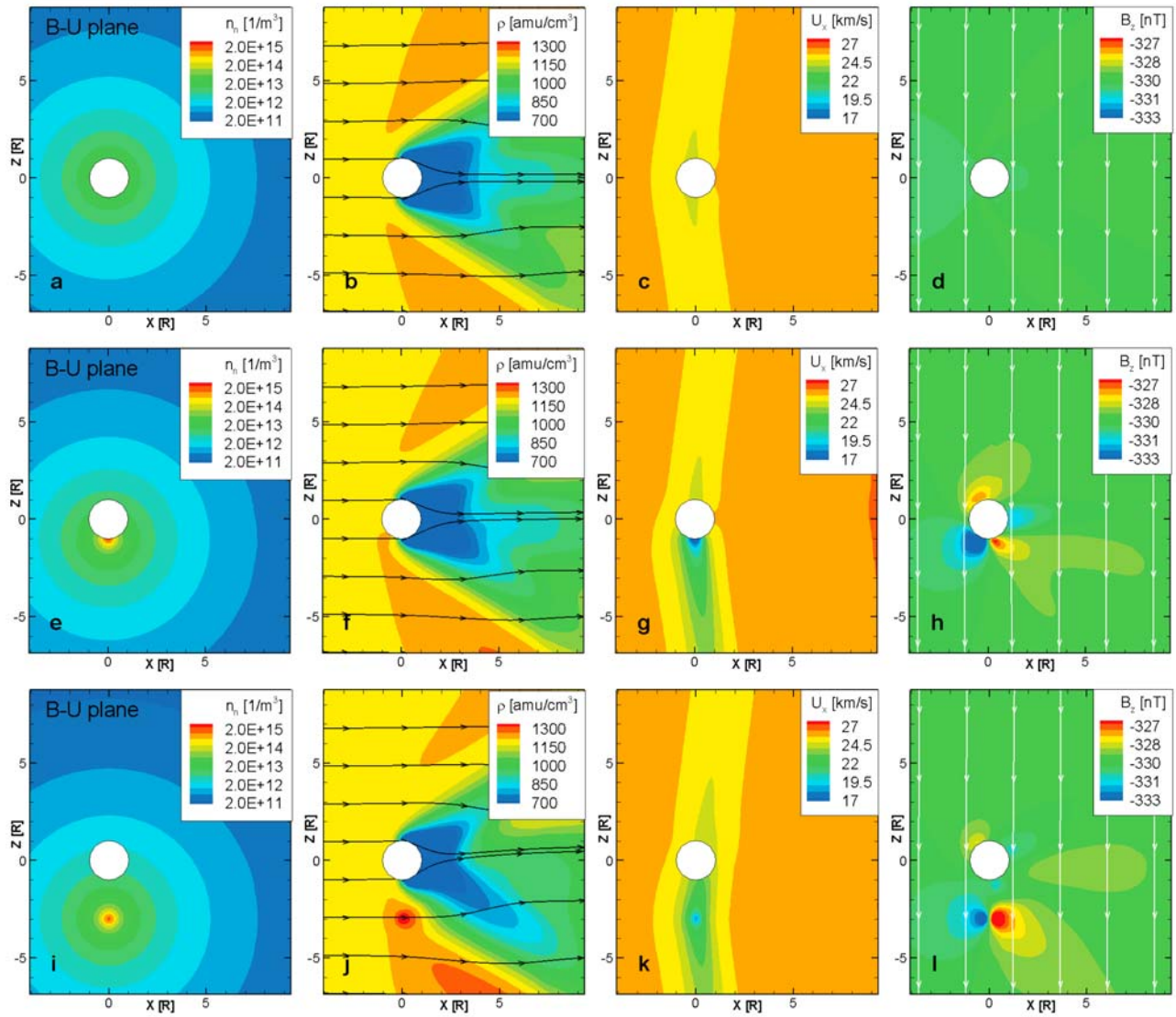

Figure 7. Two subcases compared with Case 4, showing in the $y = 0$ plane the neutral density, ion density, u_x, and magnetic field z components. Figures 7a, 7b, 7c, and 7d show the original Case 4 result. The only modification of the two subcases is the neutral density, as shown in Figures 7e and 7i. Black lines are stream lines; white lines are magnetic field lines.

nitude smaller than that at the density peak. Shown by the stream lines in Figures 7f and 7j, strong u_z flow is created in the body wake. Due to the displacement of the mass loading center below the body, the B_x perturbation is negative in the body wake. Thus when the expanding flow pushes the field in the $+z$ direction, a compression of the field lines results in the moon wake (light blue region). The associated decrease of field magnitude can be seen in the two orange regions. Comparing between Figure 7h and 7l, the detachment of the neutral peak from the moon surface causes more kinks in the field lines in this region.

[68] When studying the Cassini magnetometer observations at Enceladus, *Khurana et al.* [2007] indicated that the mass loading center is 1 to 3 R_E below the moon. Our paper 2 presents more evidence and discussion, by comparing with the Cassini observations. *Saur et al.* [2007] analytically solved the currents and fields in this region, predicting a pair of surface current crossing the Enceladus surface, which is simulated by *Kriegel et al.* [2009]. Our ideal MHD code handles the field inside the body with boundary conditions, so we cannot simulate such surface currents. However, the *Saur et al.* [2007] model did not consider the B_x perturbation and the effect of u_z. The *Kriegel et al.* [2009] result has numerical noise that makes this increase/decrease unidentifiable. In addition, *Khurana et al.* [2007] has inferred that the size of the momentum-loading obstacle is several R_E in radius. We believe that by considering the wider distribution of the plasma ionosphere and adding the displacement of the momentum-loading center, the predictions of *Saur et al.* [2007] can be significantly improved.

[69] In summary, case 4, which combines the interactions simulated in cases 1, 2 and 3, is expected to exhibit perturbation signatures comparable to first three cases. The absorbing surface creates a strong flow deflection that

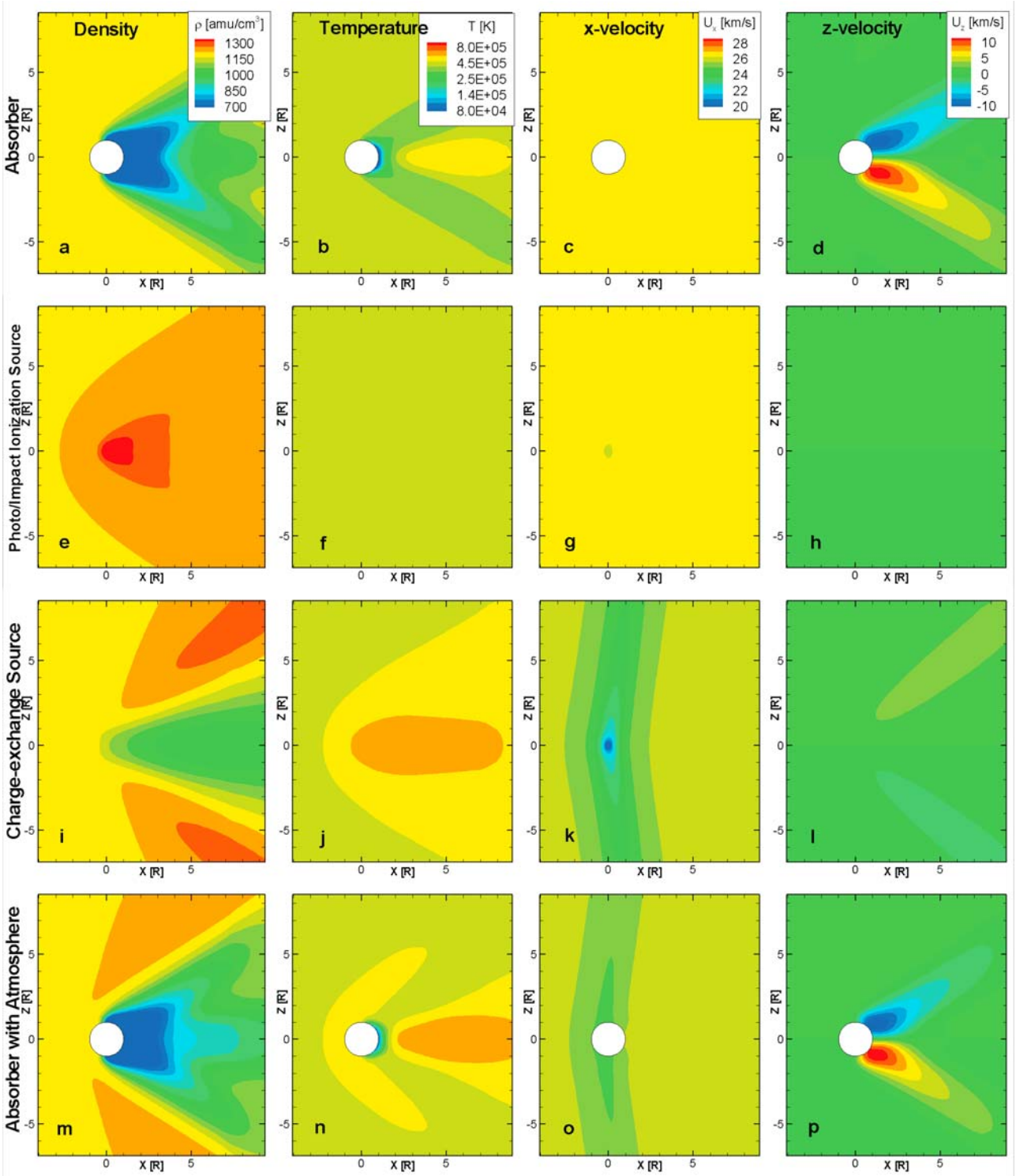

Figure 8. Cases 1 to 4, density, temperature, and velocity contours plotted in same ranges in the $y = 0$ plane (B-U plane).

overwhelms the effects of mass loading, but its perturbation on the magnetic field is weaker than that created by mass loading. This indicates that to first order, the large-scale structures that are seen by the Cassini magnetometer [*Khurana et al.*, 2007; *Jia et al.*, 2010] should be attributed to ion-neutral charge exchange around Enceladus.

3.5. Comparison Between All Four Cases

[70] The physical differences between the four cases are summarized in Table 1. The density, temperature, and velocity results of all four cases are shown side by side in Figure 8 for the $y = 0$ plane, and in Figure 9 for the $z = 0$

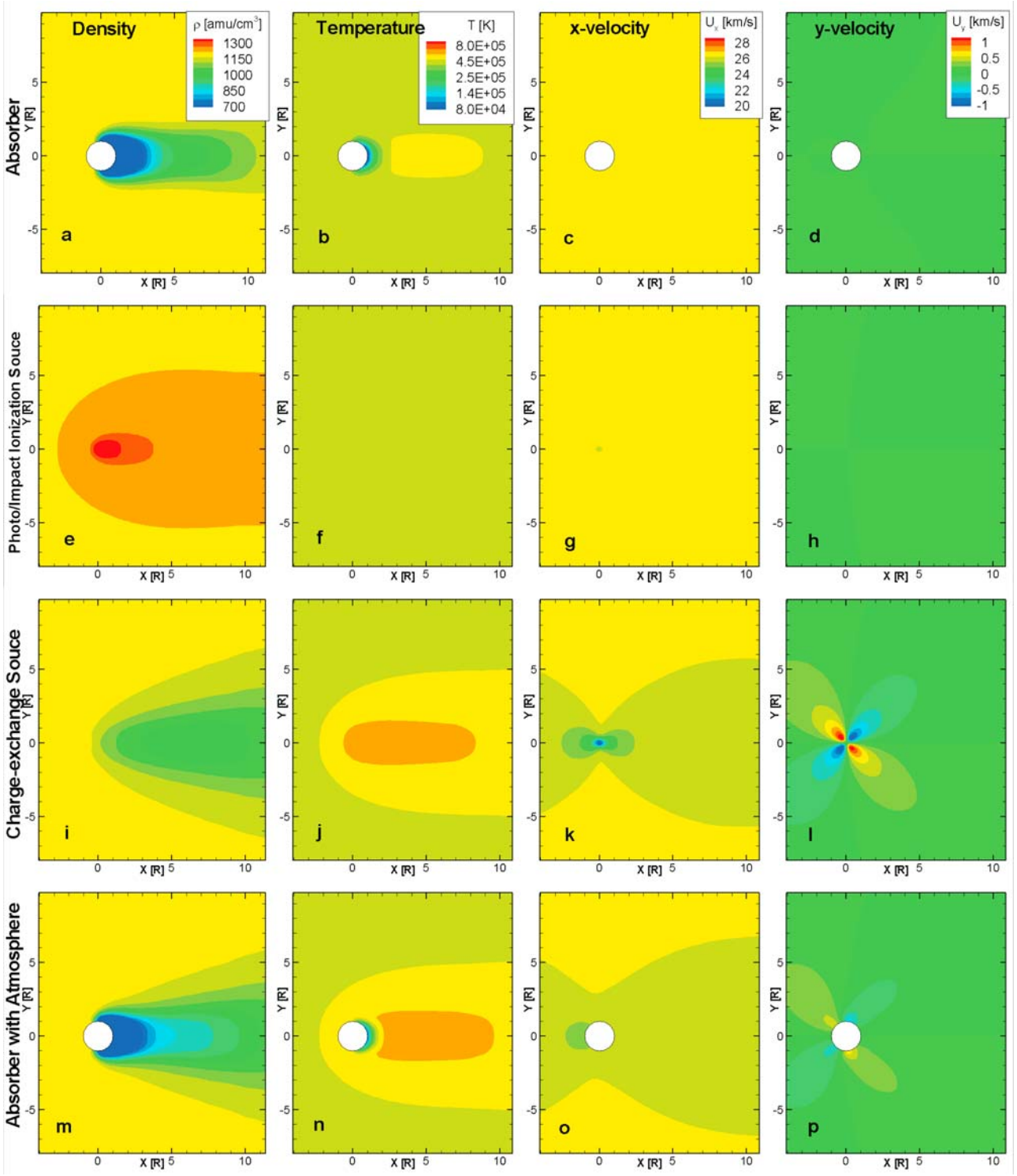

Figure 9. Cases 1 to 4, density, temperature, and velocity contours in the $z = 0$ plane, or the view along the magnetic field.

plane. For comparison, the axis, scale and contour levels are kept the same for each of the variables. Case 2 shows significantly smaller perturbation to the incident flow, indicating the significance of charge exchange in this problem. Case 3 shows a much stronger perturbation with the same shape as case 2 in velocity, while the density and temperature distributions are different. Case 4 exhibits signatures that are seen in cases 1, 2 and 3.

4. Discussion

[71] With the recent increase of observational data and development of 3-D numerical codes in various physical

regime, our understandings of interactions between plasma and nonconducting, nonmagnetic moons are deepened. Our MHD model provides a generalized solution revealing the large-scale structures. Yet there are a lot of detail not covered in this work due to the limitations of the MHD model. Intercomparison of multispecies MHD models, multifluid MHD models, anisotropic MHD models and kinetic models are needed to improve our knowledge on such interactions more precisely.

[72] The parameters used for the figures shown in this work are optimized for the plasma condition around Enceladus. Our study indicates that the general structures are not limited to Enceladus. Case 1 has been run for Tethys, Rhea and Dione conditions. Compared to the <0.3% B_z perturbation for Enceladus, the fraction of field perturbations increases with the decrease of B_z. For Tethys, Rhea and Dione, these perturbations are approximately 1%, 5% and 12%. Adding weak mass loading to these moons results in comparable results to both case 1 and case 4, but with weak mass loading applicable to these moons, the effect of absorbing body is more dominant than the mass loading. This is consistent with the findings by *Simon et al.* [2009]. More focused work, with other types of simulations, such as nonisotropic and multifluid MHD, Hall MHD, hybrid or full kinetic models are still needed on the field and plasma perturbations by varying densities of thin atmospheres. It should be noted that in comparing the B_z perturbation shown in the x–y plane in case 1 and case 4, we cannot exclude the existence of a weak mass loading source around Tethys or Rhea by the magnetometer data from the current Cassini flybys [*Khurana et al.*, 2008]. A close upstream flyby (<1 R_m) would be helpful in quantifying the upper limit of mass loading.

[73] Although the four ideal cases studied here are too simplified to be directly compared with the Enceladus observations, they provide the fundamental understandings of such plasma interaction regions before we move on to the comprehensive effect of these simple interactions coupled with each other. In addition, the study of only the Enceladus body shows that the perturbation strength by the body itself is orders of magnitude smaller than the magnetometer observations, leading to the need for a plume to explain these observations, as presented by *Khurana et al.* [2007]. Such plume studies, as presented in paper 2, in turn better constrain the Enceladus plume.

[74] Observations show that Enceladus is an icy moon that does not have a conducting surface. Compared with the magnetometer data, our model results also suggest that the Enceladus surface is well modeled with an inner boundary condition as used for cases 1 and 4. This also indicates that Enceladus does not have a global ionosphere, which is consistent with previous studies.

[75] In our model result, case 4 is a combination of cases 1, 2 and 3. On the upstream side and in the Alfven wings, the perturbation is more like the effect in case 3, while in the wake it is the rarefaction in case 1 that is dominant. Close to the tail side of the surface, the magnetic field shows a combined 3-D effect of both field rarefaction in the x direction and field pileup in the y direction. The balance of these signatures largely depends on the flow conditions, including the upstream flow and the density escaping the wake side body. A water plume extending under the south pole of Enceladus was imaged during E2, the third flyby [*Porco et al.*, 2006; *Spencer et al.*, 2006]. Such a plume has a great impact on the Saturnian system, not only in its geological effects [*Porco et al.*, 2006; *Spahn et al.*, 2006], but also for its effects on the Saturnian magnetosphere [*Dougherty et al.*, 2006; *Kivelson*, 2006]. The details of the plume configuration are discussed and constrained in an accompanying paper [*Jia et al.*, 2010].

[76] The real Enceladus-magnetosphere interaction is also different from previously studied moon-magnetosphere interaction cases, not only because of differences in flow conditions, but also because of the asymmetric mass loading source controlled by the plume. However, by simplifying this environment into these four ideal cases, we not only validate our model but also enable the comparison of the Enceladus interaction to that of other moons in such a submagnetosonic environment with the presence of a background magnetic field.

[77] **Acknowledgments.** This work at UCLA is supported by the National Aeronautics and Space Administration under JPL contract 1236948. The computer simulations are done on NASA supercomputer Columbia. The authors thank the two reviewers for their help in improving the text.

[78] Wolfgang Baumjohann thanks Sven Simon and another reviewer for their assistance in evaluating this paper.

References

Bagenal, F. (1997), The ionization source near Io from Galileo wake data, *Geophys. Res. Lett.*, *24*, 2111–2114, doi:10.1029/97GL02052.

Benz, A. O. (Ed.) (1993), *Plasma Astrophysics: Kinetic Processes in Solar and Stellar Coronae*, *Astrophys. Space Sci. Libr.*, vol. 184, Kluwer Acad., Dordrecht, Netherlands.

Birch, P. C., and S. C. Chapman (2001), Particle-in-cell simulations of the lunar wake with high phase space resolution, *Geophys. Res. Lett.*, *28*, 219–222, doi:10.1029/2000GL011958.

Burger, M. H., E. C. Sittler, R. E. Johnson, H. T. Smith, O. J. Tucker, and V. I. Shematovich (2007), Understanding the escape of water from Enceladus, *J. Geophys. Res.*, *112*, A06219, doi:10.1029/2006JA012086.

Cravens, T. E., and T. I. Gombosi (2004), Cometary magnetospheres: A tutorial, *Adv. Space Res.*, *33*, 1968–1976, doi:10.1016/j.asr.2003.07.053.

Cravens, T. E., J. U. Kozyra, A. F. Nagy, T. I. Gombosi, and M. Kurtz (1987), Electron impact ionization in the vicinity of comets, *J. Geophys. Res*, *92*, 7341–7353.

Delamere, P. A., F. Bagenal, V. Dols, and L. C. Ray (2007), Saturn's neutral torus versus Jupiter's plasma torus, *Geophys. Res. Lett.*, *34*, L09105, doi:10.1029/2007GL029437.

Dougherty, M. K., K. K. Khurana, F. M. Neubauer, C. T. Russell, J. Saur, J. S. Leisner, and M. E. Burton (2006), Identification of a dynamic atmosphere at Enceladus with the Cassini magnetometer, *Science*, *311*, 1406–1409, doi:10.1126/science.1120985.

Gombosi, T. I., D. L. De Zeeuw, R. M. Häberli, and K. G. Powell (1996), Three-dimensional multiscale MHD model of cometary plasma environments, *J. Geophys. Res.*, *101*, 15,233–15,252, doi:10.1029/96JA01075.

Haberli, R. M., M. R. Combi, T. I. Gombosi, D. L. de Zeeuw, and K. G. Powell (1997), Quantitative analysis of H_2O^+ coma images using a multiscale MHD model with detailed ion chemistry, *Icarus*, *130*, 373–386, doi:10.1006/icar.1997.5835.

Hansen, C. J., L. Esposito, A. I. F. Stewart, J. Colwell, A. Hendrix, W. Pryor, D. Shemansky, and R. West (2006), Enceladus' water vapor plume, *Science*, *311*, 1422–1425, doi:10.1126/science.1121254.

Hansen, C. J., et al. (2008), Water vapour jets inside the plume of gas leaving Enceladus, *Nature*, *456*, 477–479, doi:10.1038/nature07542.

Hansen, K. C., T. Bagdonat, U. Motschmann, C. Alexander, M. R. Combi, T. E. Cravens, T. I. Gombosi, Y.-D. Jia, and I. P. Robertson (2007), The plasma environment of comet 67P/Churyumov-Gerasimenko throughout the Rosetta main mission, *Space Sci. Rev.*, *128*, 133–166, doi:10.1007/s11214-006-9142-6.

Huebner, W. F., J. J. Keady, and S. P. Lyon (1992), Solar photo rates for planetary atmospheres and atmospheric pollutants, *Astrophys. Space Sci.*, *195*, 1–289.

Huntress, W. T., Jr. (1977), Laboratory studies of bimolecular reactions of positive ions in interstellar clouds, in comets, and in planetary atmospheres of reducing composition, *Astrophys. J. Suppl. Ser.*, *33*, 495–514, doi:10.1086/190439.

Jia, Y.-D., M. R. Combi, K. C. Hansen, and T. I. Gombosi (2007), A global model of cometary tail disconnection events triggered by solar wind magnetic variations, *J. Geophys. Res.*, *112*, A05223, doi:10.1029/2006JA012175.

Jia, Y. D., M. R. Combi, K. C. Hansen, T. I. Gombosi, F. J. Crary, and D. T. Young (2008), A 3-D global MHD model for the effect of neutral jets during the Deep Space 1 Comet 19P/Borrelly flyby, *Icarus*, *196*, 249–257, doi:10.1016/j.icarus.2008.03.010.

Jia, Y. D., C. T. Russell, K. K. Khurana, Y. J. Ma, and T. I. Najib, D. Gombosi (2010), Interaction of Saturn's magnetosphere and its moons: 2: Shape of the Enceladus Plume, *J. Geophys. Res.*, *115*, A04215, doi:10.1029/2009JA014873.

Jones, G. H., et al. (2009), Fine jet structure of electrically charged grains in Enceladus' plume, *Geophys. Res. Lett.*, *36*, L16204, doi:10.1029/2009GL038284.

Jurac, S., R. E. Johnson, J. D. Richardson, and C. Paranicas (2001), Satellite sputtering in Saturn's magnetosphere, *Planet. Space Sci.*, *49*, 319–326.

Kabin, K., K. C. Hansen, T. I. Gombosi, M. R. Combi, T. J. Linde, D. L. DeZeeuw, C. P. T. Groth, K. G. Powell, and A. F. Nagy (2000), Global MHD simulations of space plasma environments: Heliosphere, comets, magnetospheres of planets and satellites, *Astrophys. Space Sci.*, *274*, 407–421.

Kallio, E. (2005), Formation of the lunar wake in quasi-neutral hybrid model, *Geophys. Res. Lett.*, *32*, L06107, doi:10.1029/2004GL021989.

Khurana, K. K., M. K. Dougherty, C. T. Russell, and J. S. Leisner (2007), Mass loading of Saturn's magnetosphere near Enceladus, *J. Geophys. Res.*, *112*, A08203, doi:10.1029/2006JA012110.

Khurana, K. K., C. T. Russell, and M. K. Dougherty (2008), Magnetic portraits of Tethys and Rhea, *Icarus*, *193*, 465–474, doi:10.1016/j.icarus.2007.08.005.

Kivelson, M. G. (2006), Does Enceladus govern magnetospheric dynamics at Saturn?, *Science*, *311*, 1391–1392, doi:10.1126/science.1124494.

Kriegel, H., S. Simon, J. Müller, U. Motschmann, J. Saur, K.-H. Glassmeier, and M. Dougherty (2009), The plasma interaction of Enceladus: 3D hybrid simulations and comparison with Cassini MAG data, *Planet. Space Sci.*, *57*, 2113–2122, doi:10.1016/j.pss.2009.09.025.

Lipatov, A. S., and M. R. Combi (2006), Effects of kinetic processes in shaping Io's global plasma environment: A 3D hybrid model, *Icarus*, *180*, 412–427, doi:10.1016/j.icarus.2005.08.012.

Lipatov, A. S., U. Motschmann, and T. Bagdonat (2002), 3D hybrid simulations of the interaction of the solar wind with a weak comet, *Planet. Space Sci.*, *50*, 403–411.

Ma, Y., A. F. Nagy, T. E. Cravens, I. V. Sokolov, K. C. Hansen, J.-E. Wahlund, F. J. Crary, A. J. Coates, and M. K. Dougherty (2006), Comparisons between MHD model calculations and observations of Cassini flybys of Titan, *J. Geophys. Res.*, *111*, A05207, doi:10.1029/2005JA011481.

Neubauer, F. M. (1980), Nonlinear standing Alfven wave current system at Io—Theory, *J. Geophys. Res.*, *85*, 1171–1178, doi:10.1029/JA085iA03p01171.

Porco, C. C., et al. (2006), Cassini observes the active south pole of Enceladus, *Science*, *311*, 1393–1401, doi:10.1126/science.1123013.

Powell, K. G., P. L. Roe, T. J. Linde, T. I. Gombosi, and D. L. D. Zeeuw (1999), A solution-adaptive upwind scheme for ideal magnetohydrodynamics, *J. Comput. Phys.*, *154*(2), 284–309, doi:10.1006/jcph.1999.6299.

Richardson, J. D., A. Eviatar, M. A. McGrath, and V. M. Vasyliũnas (1998), OH in Saturn's magnetosphere: Observations and implications, *J. Geophys. Res.*, *103*, 20,245–20,256, doi:10.1029/98JE01127.

Roussos, E., et al. (2008), Plasma and fields in the wake of Rhea: 3-D hybrid simulation and comparison with Cassini data, *Annales Geophysicae*, *26*, 619–637.

Russell, C. T., and D. E. Huddleston (2000), The unipolar inductor myth: Mass addition or motional electric field as the source of field-aligned currents at Io, *Adv. Space Res.*, *26*, 1665–1670, doi:10.1016/S0273-1177(00)00114-9.

Saur, J., F. M. Neubauer, D. F. Strobel, and M. E. Summers (2002), Interpretation of Galileo's Io plasma and field observations: I0, I24, and I27 flybys and close polar passes, *J. Geophys. Res.*, *107*(A12), 1422, doi:10.1029/2001JA005067.

Saur, J., F. M. Neubauer, and N. Schilling (2007), Hemisphere coupling in Enceladus' asymmetric plasma interaction, *J. Geophys. Res.*, *112*, A11209, doi:10.1029/2007JA012479.

Saur, J., N. Schilling, F. M. Neubauer, D. F. Strobel, S. Simon, M. K. Dougherty, C. T. Russell, and R. T. Pappalardo (2008), Evidence for temporal variability of Enceladus' gas jets: Modeling of Cassini observations, *Geophys. Res. Lett.*, *35*, L20105, doi:10.1029/2008GL035811.

Simon, S., J. Saur, F. M. Neubauer, U. Motschmann, and M. K. Dougherty (2009), Plasma wake of Tethys: Hybrid simulations versus Cassini MAG data, *Geophys. Res. Lett.*, *36*, L04108, doi:10.1029/2008GL036943.

Spahn, F., et al. (2006), Cassini dust measurements at Enceladus and implications for the origin of the E ring, *Science*, *311*, 1416–1418, doi:10.1126/science.1121375.

Spencer, J. R., et al. (2006), Cassini encounters Enceladus: Background and the discovery of a south polar hot spot, *Science*, *311*, 1401–1405, doi:10.1126/science.1121661.

Spitale, J. N., and C. C. Porco (2007), Association of the jets of Enceladus with the warmest regions on its south-polar fractures, *Nature*, *449*, 695–697, doi:10.1038/nature06217.

Spreiter, J. R., and A. Y. Alksne (1970), Solar-wind flow past objects in the solar system., *Annu. Rev. Fluid Mech.*, *2*, 313–354, doi:10.1146/annurev.fl.02.010170.001525.

Tokar, R. L., et al. (2006), The interaction of the atmosphere of Enceladus with Saturn's plasma, *Science*, *311*, 1409–1412, doi:10.1126/science.1121061.

Tóth, G., et al. (2005), Space Weather Modeling Framework: A new tool for the space science community, *J. Geophys. Res.*, *110*, A12226, doi:10.1029/2005JA011126.

Vasyliunas, V. M. (2008), Comparing Jupiter and Saturn: Dimensionless input rates from plasma sources within the magnetosphere, *Ann. Geophys.*, *26*, 1341–1343.

Waite, J. H., et al. (2006), Cassini Ion and Neutral Mass Spectrometer: Enceladus plume composition and structure, *Science*, *311*, 1419–1422, doi:10.1126/science.1121290.

T. I. Gombosi and G. Toth, Department of Atmospheric, Oceanic and Space Sciences, University of Michigan, Ann Arbor, MI 48109, USA.

Y.-D. Jia, K. K. Khurana, J. S. Leisner, and C. T. Russell, IGPP, University of California, Los Angeles, CA 90095, USA. (yingdong@ucla.edu)